Two-quantum 2D FT electronic spectroscopy of biexcitons in GaAs quantum wells

Katherine W. Stone[1], Kenan Gundogdu[1], Daniel B. Turner[1],

Xiaoqin Li[2], Steven T. Cundiff[3], and Keith A. Nelson[1,a]

Ultrafast excitation of solids creates coherent superpositions of correlated many-particle states. For electronic excitations, important high-order many-body correlations may contribute strongly to signals measured in nonlinear spectroscopy, but often the contributions are highly convolved with those from lower-order correlations. Using a novel method for two-quantum 2D electronic Fourier transform spectroscopy, we are able to isolate signals from high-order correlations and record direct observations of many-body dynamics in semiconductor quantum wells.

Two-dimensional Fourier transform spectroscopy (2D FTS), long used in nuclear magnetic resonance (NMR) to unravel structure and dynamics in systems with multiple, interacting nuclear spins, has recently emerged in the infrared and optical spectral regions as a powerful approach to the study of complex systems with multiple vibrational and electronic transitions respectively (*1-5*). Coherent electronic 2D FTS is particularly well suited for the study of photosynthetic antenna complexes (*6*) and semiconductor nanostructures (*7*) because of their multiple exciton states among which electronic coherence and energy transport occur. In semiconductors, great additional complexity arises due to long-range many-body interactions among excitons. These interactions,

---

[1] Department of Chemistry, Massachusetts Institute of Technology, Cambridge, MA 02139-4307 USA
[2] Department of Physics, University of Texas at Austin, Austin, TX 78712-0264 USA
[3] JILA, University of Colorado and National Institute of Standards and Technology
Boulder, CO 80309-0440 USA
[a]Author to whom correspondence should be addressed: *kanelson@mit.edu*

which are evident from distinctive signals at both positive and negative probe delays in time-resolved measurements (*8-11*), can be understood phenomenologically in terms of modifications of exciton properties through local field effects (*10, 11*), excitation-induced dephasing (*12, 13*) and excitation-induced frequency shifts (*14*), and in terms of the formation of entirely new quasiparticles, biexcitons (*15*), which are bound complexes of two correlated excitons analogous to diatomic molecules. All of these phenomena arise naturally in a full many-body theory starting from the Hamiltonian for the interacting electrons and keeping correlation terms beyond a Hartree-Fock approximation (*16*). Ultrafast electronic 2D FTS has enabled rigorous comparison of distinct many-body effects by isolating them in distinct experimental features and by providing exciton phase information (*17, 18*). However, direct time-resolved observations of biexcitons have been elusive because there has not been any optical analog of multiple-quantum 2D NMR, in which two-quantum spin coherences are excited by two successive radiofrequency (RF) fields, allowed to evolve, and observed by a third RF field that converts them to one-quantum coherences from which signal is radiated. Indeed, no such analog would be possible in electronic 2D FTS as it has been conducted ordinarily because the four non-collinear optical beams that arrive at the sample (including a "local oscillator" (LO) beam used for interferometric detection of the radiated signal field) are not fully phase coherent. Two pairs of phase-related optical beams are used, but there is no controlled phase relationship between the pairs. Thus coherent evolution in time intervals between the pulses of each pair can be correlated, but only incoherent evolution during time periods between pulses of different pairs may be examined. Extending ultrafast electronic 2D FTS to include two-quantum coherences, which are studied routinely in NMR, will greatly enhance its versatility by allowing access to biexcitons and other multiply excited states that are "dark" to one-photon transitions and by providing an additional conjugate frequency axis along which complex spectra can be spread out. Furthermore, multiple-quantum coherences are often involved in coherent control schemes (*19*) for quantum information processing (*20*), accessing exciton spin coherences (*21*) and controlling electromagnetically induced transparency in semiconductors (*22*); thus their decoherence

rates are important for practical as well as fundamental reasons. While two-quantum 2D FTS of molecular vibrational overtones has been demonstrated in the infrared spectral region (*23*), where the wavelength is long enough that the phases of the IR fields in four distinct beams can be maintained without extraordinary measures, a comparable measurement in the visible region is far more demanding.

Recently we showed that spatiotemporal femtosecond pulse shaping, in which a single beam of light with a single ultrashort pulse is transformed into multiple beams with single or multiple pulses, provides the basis for fully coherent multidimensional electronic spectroscopy (*24*). The pulse shaper generates and controls the timing and optical phases of all the pulses in each beam so coherent evolution may be examined during any of the specified time periods between pulses in any beam. Here we present the first application of this methodology to the direct observation and separation of two-quantum biexciton coherences and interaction-induced coherences in a quantum well structure which are correlations not treated within a Hartree-Fock approximation. The present observations and the dephasing information extracted from them are distinct from those associated with one-quantum exciton-biexciton coherences observed in earlier 2D FTS measurements as partially resolved shoulders on the excitonic peaks (*18, 25*). They also are distinct from frequency-domain measurements on single quantum dots (*26*) in which two-quantum pathways yield linewidths with contributions from both exciton and biexciton dephasing rates from which deconvolution may yield the latter. And unlike previous time-integrated FWM experiments using two-quantum pathways (*27, 28*), our measurements track the two-quantum phase evolutions at optical frequencies and correlate them to optical one-quantum coherences. Our two-quantum 2D FTS experiments separate the two-quantum coherences that arise from multi-exciton interactions, such as biexciton formation and interaction-induced coherences, allowing the phenomena to be studied even when their signatures cannot be separated spectrally.

The experimental setup is shown in Fig. 1. The output of a femtosecond Ti:Sapphire oscillator was directed through a passive spatial shaping element to form the four beams needed for the fields E_A, E_B, E_C, and E_{LO}. The beams were directed into the

spatiotemporal pulse shaper, which includes a grating and a two-dimensional liquid crystal spatial light modulator (SLM) that independently controls the amplitudes and optical phases of the dispersed frequency components (*29*). The shaped fields were directed into the sample in a non-collinear phase-matching geometry that permits selection of a small subset of potential contributions to the signal because the signal emerges from the sample as a coherent beam in a direction (collinear with the LO) given by the wavevector matching condition $k_{sig} = k_A + k_B - k_C$.

The sample consisted of ten layers of 10 nm thick GaAs, separated by 10 nm thick barriers of $Al_{0.3}Ga_{0.7}As$, and was held at a temperature of 10 K. The optically excited carrier density was varied from 10^9 to 10^{11} carriers per cm^2 per well. A neutral density filter was used to reduce the LO beam power to 10^{-3} of the others. The relevant heavy-hole (HH) and light-hole (LH) exciton and biexciton energy levels are shown in Fig. 2A. The sequence of fields applied in order to examine the biexciton coherence which evolved during the two-quantum coherence (2QC) period, τ_2, is shown in Fig. 2B. The double-sided Feynman diagram that illustrates the sample response of primary interest is shown in Fig. 2C(i). The polarizations of the input beams, controlled via individual quarter-wave plates, selected whether homogeneous (HH-HH and LH-LH) or mixed (HH-LH) biexcitons were observed. For instance, the HH-HH biexciton was observed when the first circularly-polarized resonant field, E_A, produced a "spin-up" HH exciton-ground state coherence, with wavevector k_A, which evolved during the one-quantum coherence (1QC) period, τ_1, and the second oppositely ("cross") circularly-polarized field, E_B, converted the coherence to a two-quantum biexciton-ground state coherence with wavevector k_A+k_B that underwent coherent oscillations during τ_2. The biexciton-ground state coherence frequency, ω_b, is given by the biexciton energy $E_b = \hbar\omega_b = 2\varepsilon_e -$

ε_B where ε_e is the exciton energy and ε_B the biexciton binding energy. A third circularly-polarized field, E_C, regenerated a one-quantum HH exciton coherence with wavevector $k_A+k_B-k_C$ whose signal field radiated during time t was overlapped spatially with that of the cross-circularly polarized reference field E_{LO} and directed into a spectrometer for spectral interferometry analysis (*30*). The pulse shaper was used to control the relative

time delays of the pulses in all four fields. The time delays of the pulse envelopes can be varied without varying the optical phases, a key capability that permits the equivalent of rotating frame detection in NMR. A fully coherent three-dimensional measurement can be carried out to determine the complex signal as a function of all three time intervals τ_1, τ_2 and t, or through Fourier transformation, the corresponding variables ω_1, ω_2 and ω. In the present 2D measurements, τ_1 was set to zero and the signal field dependence on the emission frequency ω was determined at a specified 2QC delay time τ_2 directly through spectral interferometry with the arrival time of the E_{LO} pulse set to 1 ps prior to the E_C pulse. The determination was repeated as τ_2 was varied in 16-fs steps, and Fourier transformation with respect to τ_2 was conducted to yield the signal field dependence on the 2QC frequency, ω_2. The 2D surfaces presented in this work are the magnitudes of the complex fields as functions of the 2QC and emission frequencies, ω_2 and ω. The emission frequency is presented in the rotating frame by subtracting the user-defined carrier frequency, ω_0, which is the frequency component of the pulse that is given zero phase shift by the pulse shaper for all pulses and all delays.

Another signal contribution expected in our measurements from biexciton-ground state coherences is indicated in Figure 2C(ii). As in 2C(i), the first two fields yield biexciton coherences with wavevector k_A+k_B that evolve during τ_2, but in this case the third field E_C generates new exciton coherences with wavevector k_C from the ground state. Signal with wavevector $k_A+k_B-k_C$ is radiated during t through exciton-biexciton coherences whose frequency ω_{eb} is expected to be red-shifted from the exciton coherence frequency, ω_e, due to the biexciton binding energy, i.e. $\omega_{eb} = \omega_e - \varepsilon_B^{eb}/\hbar$ where we have superscripted the binding energy for reasons that will become evident. In contrast, other contributions to the two-quantum signal cannot be assigned to standard double-sided Feynman diagrams that are used to describe the responses of non-interacting systems such as atoms or molecules because they do not arise from the newly formed biexciton state. Rather they result solely from the many-body processes discussed above induced by the first two pulses. This is most intuitive when explained in the context of the local-field model, although excitation-induced dephasing and frequency-shift contribute as

well. Specifically, a single pulse induces a linear macroscopic polarization in the sample that is driven not only by the applied field, but also by a local field that arises due to Coulomb interactions among the excited carriers. This local field exists without the presence of the applied field and therefore has long been used to explain the signal at negative delay in two-pulse four-wave mixing experiments (*11, 31, 32*). Two such interactions not only cause this signal to decay twice as fast as the exciton dephasing rate, but to oscillate with twice the exciton resonance frequency (with no binding energy correction since these oscillations do not involve biexcitons) during τ_2 which we observe in our measurements. We explain this in more detail in the Supplementary Information section.

All of these signals require many-body interactions typical of condensed phase systems. Many-body effects were revealed in time-resolved four-wave mixing signals at negative delay times (*9-11*) prior to the advent of electronic 2D FTS, but 2D measurements are necessary to separate and characterize the distinct contributions. Our arrangement of pulse arrival times and wavevectors ("SIII" in nonlinear spectroscopic terminology (*33*)) can be thought of as having a negative delay time with respect to the more usual two-pulse photon echo ("SI") arrangements in which the conjugate pulse (i.e. the negative wavevector contributor to the signal, E_C) arrives first to generate a sample response.

The emission spectrum measured in the phase-matched direction when all the excitation fields were time-coincident is plotted in Fig. 3A along with the laser pulse spectrum. The HH and LH exciton transition frequencies are 372.2 and 373.7 THz (1.539 and 1.546 eV), respectively. The 2D surface determined from the magnitude of the full signal field under cross-circular excitation, Fig 3B, shows the HH-HH biexciton coherence. The carrier density was 7×10^{10} per cm^2 per well. Note that the spectral interferometry measurement gives the signal field as a function of the absolute emission frequency, so we have subtracted the carrier frequency (368.0 $\pm$ 0.05 THz) from the emission frequency in order to present both frequency axes in the rotating frame. Along the emission frequency axis, ω, the HH-HH biexciton peak (*a*) appears as expected at the

6

HH exciton emission frequency (4.27 THz higher than the carrier frequency.) Along the 2QC frequency axis, ω_2, it appears at 8.33 ± 0.02 THz relative to the carrier frequency. This is the first determination of the biexciton energy through direct observation of the ground state-biexciton coherence frequency. The value is less than twice the HH exciton emission frequency, yielding a biexciton binding energy of $\varepsilon_B = 0.77 \pm 0.43$ meV (*34*).

The exciton-biexciton coherence (*b*), described by the Feynman pathway in 2C(ii), appears as a shoulder of the biexciton peak slightly red-shifted in ω. A least-squares two-Lorentzian fit to the main peak and the shoulder as functions of ω yields the exciton-biexciton frequency ω_{eb}, and the difference between this and the main peak emission frequency ω_e yields a biexciton binding energy ε_B^{eb} of 1.49 ± 0.03 meV. The binding energy obtained in this manner is in closer agreement to previously calculated and observed values (*35-39*) that also were measured from differences between the frequencies of ground state-exciton and exciton-biexciton coherences. However, the binding energy value ε_B^{eb} depends on the exciton-biexciton transition which weights subsets of the correlated two-particle (exciton) and four-particle (biexciton) states that may not reflect the precise energies of either. The linewidth of a Lorentzian least-squares fit to peak *a* as a function of ω_2 yields a HH-HH biexciton dephasing time of 2.08 ± 0.11 ps during τ_2. This is the first report of a biexciton dephasing time in GaAs quantum wells. Figure 4 shows a previously undiscovered dependence of the biexciton dephasing time on the excitation density. The observed excitation-induced biexciton dephasing effects occur due to six-particle correlations (interactions between biexcitons and excitons). Correlations of this order have been observed in previous nonlinear spectroscopy measurements (*40*), but only in a highly convolved manner without isolation of their distinct effects. The biexciton energy was found to be essentially independent of excitation density. We note that the LH exciton transition dipole is one-third that of the HH exciton, so the LH-LH biexciton feature is too weak to be seen in the 2D FT spectra presented here.

Results of measurements conducted at the same carrier density with co-circularly polarized pulses are shown in Fig. 3C with features denoted *c, d* and *e*. The mixed biexciton-ground state coherence (*c*) is observed directly for the first time. Its position along the ω_2 axis is 9.71 ± 0.01 THz, indicating a HH-LH biexciton binding energy of 1.39 ± 0.46 meV. This is larger than the HH-HH biexciton binding energy, as expected since the binding energy is known to increase for decreasing electron-hole mass ratio and the light hole has a larger in-plane mass (*41*). A red-shifted emission shoulder (*d*), analogous to the shoulder (*b*) seen in the cross-circularly polarized case, appears, but in this case it is not sufficiently distinct to yield an accurate biexciton-exciton emission peak frequency. The mixed biexciton dephasing time is 1.03 ± 0.05 ps and, like the HH biexciton, it decreases for increasing carrier density. See Fig. 4. The mixed biexcitons, which are bound states formed from the correlations of opposite-spin HH and LH excitons, are found to emit only at the LH exciton frequency, even though emission at the HH exciton frequency is expected. This is likely due to interference with emission at the same frequency (*42*), from feature (*e*) which, centered at twice the HH exciton frequency in ω_2, is solely the result of many-body interactions that cannot be described in terms of double-sided Feynman diagrams, as discussed earlier. Although not visible in the data as displayed in Fig. 3C, there is also a very weak interaction-induced signal at twice the LH exciton transition frequency. The deconvolved 2QC transients for the HH-HH and mixed biexcitons and the HH exciton interaction-induced effect are compared in Fig. S1 of the supplementary section. When comparing these measurements to traditional transient FWM experiments (see Fig. S2) it is clear that the phase-sensitivity and spectral separation of 2D FTS data provide a much clearer picture of the higher-order Coulomb correlations involved.

We performed several additional measurements, some presented in the supplementary section, whose results support our interpretations. First, we reduced the carrier frequency by several THz and found that the increase in the biexciton 2QC frequency was twice the change in carrier frequency, as shown in Fig. S3 of the

supplementary section. In 2D FT photon echo (SI) measurements that we will report in detail subsequently, we observe red-shifted emission lineshapes of the cross-peaks. These cross-peaks indicate coupling between the HH and LH valence bands through the conduction band, and the red-shifted lineshape indicates emission through a biexciton-exciton coherence. However, this feature is only observed in the LH exciton emission, which supports the mixed biexciton SIII results (Fig. 3C) presented here. We also fixed τ_1 at various nonzero values and recorded 2D spectra that showed the same features seen in Fig. 3B and 3C. These data presented as a function of all three frequency dimensions constitute a full 3D FT spectrum.

The two-quantum 2D FT measurements presented here show direct evidence for multi-exciton states (*25, 43*), including mixed biexcitons formed from HH and LH excitons. Comprehensive analysis of the real and imaginary parts of the complex 2D FT spectra will provide further insight into the many-body effects in this prototype system. More complex nanostructures also will be of interest. In semiconductor double and multiple quantum wells, coherence and energy transfer among excitons and biexcitons in different wells should be observable directly. In quantum dots, observation of multiple-quantum coherences from biexcitons and higher-lying states should prove possible. These states have additional importance in QD laser gain and other applications. The two-quantum coherences observed here demonstrate the unique capabilities of fully phase-coherent multidimensional FT electronic spectroscopy and the simplicity of the spatiotemporal pulse-shaping approach. In general, it should be possible to use two-quantum 2D FT electronic spectroscopy to access 'dark' states using multiple-photon transitions. The same apparatus and measurements can be used for feedback-directed quantum control over the coherences involved. We are progressing toward consummation of the marriage of multiple-pulse FT NMR, with its multidimensional frequency selectivity based on arbitrary waveform generation, and multiple-beam nonlinear optical spectroscopy, with its wavevector selectivity based on phase-matching (*44*).

References

1. M. C. Asplund, M. T. Zanni, R. M. Hochstrasser, *Proc. Nat. Acad. Sci.* **97**, 8219 (2000).
2. H. S. Chung, M. Khalil, A. Tokmakoff, *J. Phys. Chem. B* **108**, 15332 (2004).
3. M. L. Cowan, J. P. Ogilvie, R. J. D. Miller, *Chem. Phys. Lett.* **386**, 184 (2004).
4. D. M. Jonas, *Annu. Rev. Phys. Chem.* **54**, 425 (2003).
5. P. F. Tian, D. Keusters, Y. Suzaki, W. S. Warren, *Science* **300**, 1553 (2003).
6. G. S. Engel *et al.*, *Nature* **446**, 782 (2007).
7. C. N. Borca, T. Zhang, X. Li, S. T. Cundiff, *Chem. Phys. Lett.* **416**, 311 (2005).
8. J. A. Bolger, A. E. Paul, A. L. Smirl, *Phys. Rev. B* **54**, 11666 (1996).
9. K. Bott *et al.*, *Phys. Rev. B* **48**, 17418 (1993).
10. K. Leo *et al.*, *Phys. Rev. Lett.* **65**, 1340 (1990).
11. M. Wegener, D. S. Chemla, S. Schmitt-Rink, W. Schafer, *Phys. Rev. A* **42**, 5675 (1990).
12. Y. Z. Hu *et al.*, *Phys. Rev. B* **49**, 14382 (1994).
13. H. Wang *et al.*, *Phys. Rev. Lett.* **71**, 1261 (1993).
14. J. M. Shacklette, S. T. Cundiff, *Phys. Rev. B* **66**, 045309 (2002).
15. R. C. Miller, D. A. Kleinman, A. C. Gossard, O. Munteanu, *Physical Review B* **25**, 6545 (1982).
16. T. Meier, P. Thomas, S. W. Koch, *Coherent Semiconductor Optics - From Basic Concepts to Nanostructure Applications* (Springer, Berlin, 2007).
17. X. Li, T. Zhang, C. N. Borca, S. T. Cundiff, *Phys. Rev. Lett.* **96**, 057406 (2006).
18. T. Zhang *et al.*, *Proc. Nat. Acad. Sci.* **104**, 14227 (2007).
19. T. Voss, I. Ruckman, J. Gutowski, V. M. Axt, T. Kuhn, *Physical Review B* **73**, 115311 (2006).
20. X. Li *et al.*, *Science* **301**, 809 (2003).
21. P. Gilliot *et al.*, *Physical Review B* **75**, 125209 (2007).
22. M. C. Phillips *et al.*, *Phys. Rev. Lett.* **91**, 183602 (2003).
23. E. C. Fulmer, P. Mukherjee, A. T. Krummel, M. T. Zanni, *J. Chem. Phys.* **120**, 8067 (2004).
24. J. C. Vaughan, T. Hornung, K. W. Stone, K. A. Nelson, *J. Phys. Chem. A* **111**, 4873 (2007).
25. L. Yang, I. V. Schweigert, S. T. Cundiff, S. Mukamel, *Phys. Rev. B* **75**, 125302 (2007).
26. G. Chen *et al.*, *Phys. Rev. Lett.* **88**, 117901(4) (2002).
27. K. B. Ferrio, D. G. Steel, *Phys. Rev. B* **54**, 5231 (1996).
28. T. Saiki, M. Kuwata-Gonokami, T. Matsusue, H. Sakaki, *Physical Review B* **49**, 7817 (1994).
29. J. C. Vaughan, T. Hornung, T. Feurer, K. A. Nelson, *Opt. Lett.* **30**, 323 (2005).
30. L. Lepetit, G. Cheriaux, M. Joffre, *J. Opt. Soc. Am. B* **12**, 2467 (1995).
31. D. S. Kim, J. Shah, T. C. Damen, L. N. Pfeiffer, W. Schafer, *Physical Review B* **50**, 5775 (1994).

32. A. L. Smirl, M. J. Stevens, X. Chen, O. Buccafusca, *Physical Review B* **60**, 8267 (1999).

33. S. Mukamel, *Principles of Nonlinear Optical Spectroscopy*, Oxford Series on Optical and Imaging Sciences (Oxford University Press, Inc., New York, 1995).

34. Note: The uncertainty in the binding energy includes the error in the Lorentzian least-squares fitting parameters and spectral dispersion over one pixel of the 2D SLM.

35. D. Birkedal, J. Singh, V. G. Lyssenko, J. Erland, J. M. Hvam, *Physical Review Letters* **76**, 672 (1996).

36. A. V. Filinov, C. Riva, F. M. Peeters, Y. E. Lozovik, M. Bonitz, *Physical Review B* **70**, 035323 (2004).

37. J.-J. Liu, X.-J. Kong, Y. Liu, *Journal of Applied Physics* **84**, 2638 (1998).

38. D. J. Lovering, R. T. Phillips, G. J. Denton, *Phys. Rev. Lett.* **68**, 1880 (1992).

39. K.-H. Pantke, D. Oberhauser, V. G. Lyssenko, J. M. Hvam, G. Weimann, *Physical Review B* **47**, 2413 (1993).

40. D. S. Chemla, J. Shah, *Nature* **411**, 549 (2001).

41. D. A. Kleinman, *Phys. Rev. B* **28**, 871 (1983).

42. L. Yang, S. Mukamel, *Physical Review B* **77**, 075335 (2008).

43. T. Meier, S. W. Koch, M. Phillips, H. Wang, *Phys. Rev. B* **62**, 12605 (2000).

SUPPLEMENTARY ONLINE MATERIAL
www.sciencemag.org

Perturbative solution of the modified Optical Bloch equations

Fig. S1

Fig. S2

Fig. S3

FIGURE CAPTIONS

Fig. 1. Fully coherent electronic 2D FT spectroscopy using a spatiotemporal pulse shaper. The laser output is focused by a spherical lens (SL1) into a phase mask (PM) whose perpendicularly oriented grating patterns produce four first-order diffracted beams that pass through a beamsplitter (BS) and into the pulse shaper consisting of a grating (G), cylindrical lens (CL), and 2D liquid crystal spatial light modulator (SLM). The frequency components of the four beams are dispersed horizontally across four distinct SLM regions. Within each region, each dispersed frequency component is diffracted (see enlargement) by a sawtooth phase pattern whose amplitude and spatial phase are used to control the frequency component's amplitude and phase. The diffracted components are recombined at the grating, yielding the four fully phase-coherent, temporally shaped fields that are reflected off the beamsplitter, spatially filtered (SF) to reject zero-order light reflected off the SLM, and focused into the quantum well (QW) sample. The spatially overlapped signal and LO beams are directed into a spectrometer for spectral interferometry analysis of the signal field. The illustration shows every optical element in the setup before the sample except for waveplates, polarizers, and a neutral density filter in the LO beam.

Fig. 2. (A) Energy level diagram illustrating the polarization selection rules for HH and LH excitons and biexcitons. Red (blue) arrows represent excitation of the HH (LH) exciton. Solid (dashed) arrows represent right-hand (left-hand) circularly polarized light. (B) Schematic illustration of the SIII four-wave mixing pulse sequence. The first pulse E_A excites exciton coherences that oscillate during the 1QC period τ_1. According to the polarization selection rules set out in (A) the second pulse E_B converts the exciton coherences to biexciton coherences which oscillate during the 2QC period, τ_2. A third-order polarization in the sample is induced by the third pulse E_C and is radiated during the emission time, t. (C) Relevant SIII Feynman pathways involving HH biexciton coherences for cross-circular excitation.

Fig. 3. (A) GaAs QW exciton emission spectrum with peaks at 372.2 and 373.7 THz from HH and LH excitons, respectively. The laser pulse spectrum is shown with the carrier frequency indicated. (B) SIII 2D signal magnitude for cross-circularly polarized pulses. The features at 4.27 and 5.77 THz along the emission frequency axis, ω, correspond to pathways in which the system evolved as HH and LH exciton coherences, respectively, during the emission time. The HH-HH biexciton coherence (*a*) is observed directly. The shoulder (*b*) is due to exciton-biexciton coherences that radiated during the emission time. (C) SIII surface for co-circular excitation. The HH-LH biexciton peak (*c*) is observed directly and exhibits a red-shifted emission lineshape (d) due to exciton-biexciton coherences. The feature (*e*) at exactly twice the HH exciton frequency in ω_2 is induced through other many-particle Coulomb interaction mediated mechanisms. The contour lines are plotted at 7% intervals.

Fig. 4. Carrier density dependence of the biexciton linewidth. As the carrier density increases, the dephasing time of the biexcitons decreases due to excitation-induced dephasing (EID).
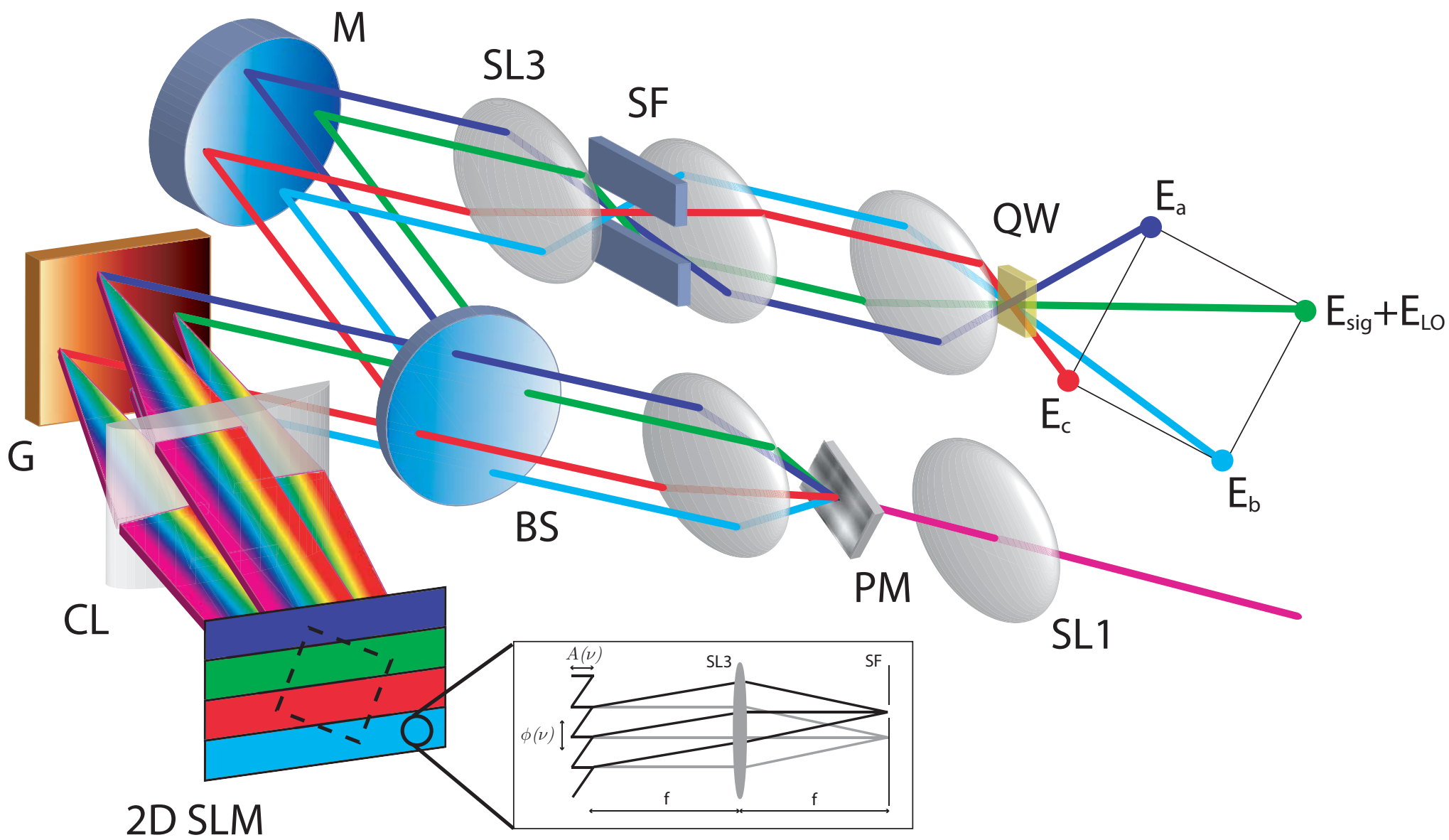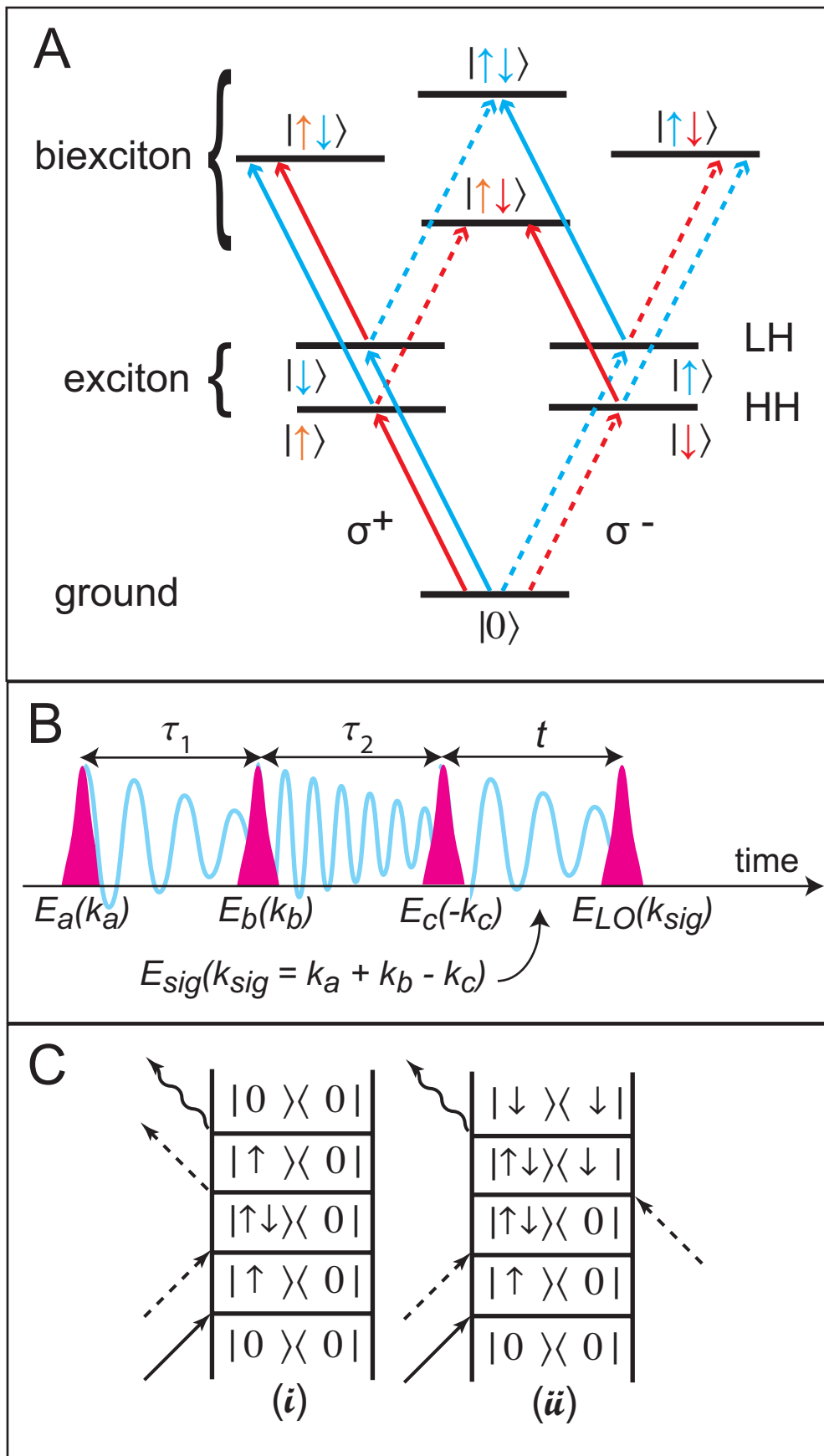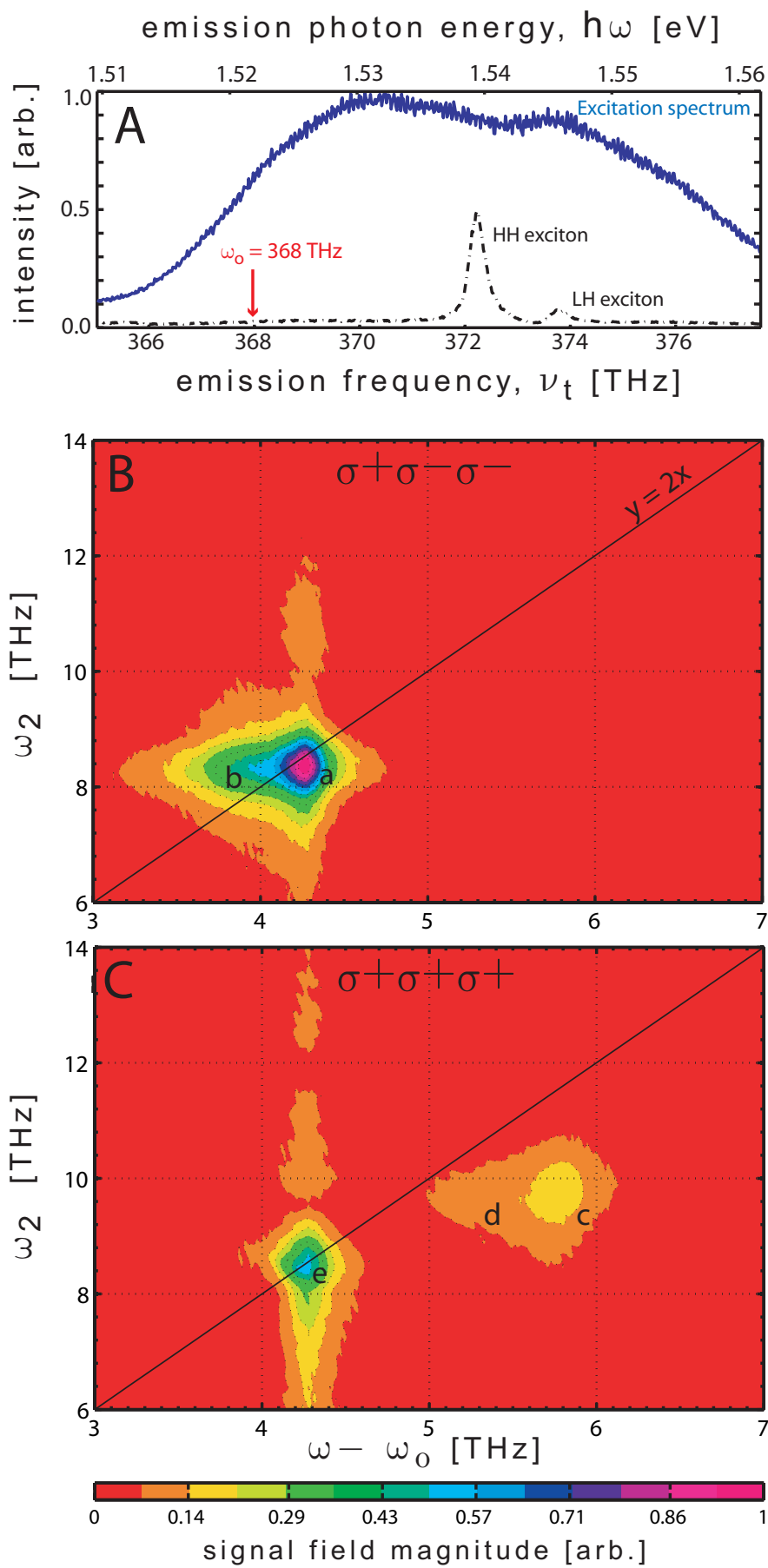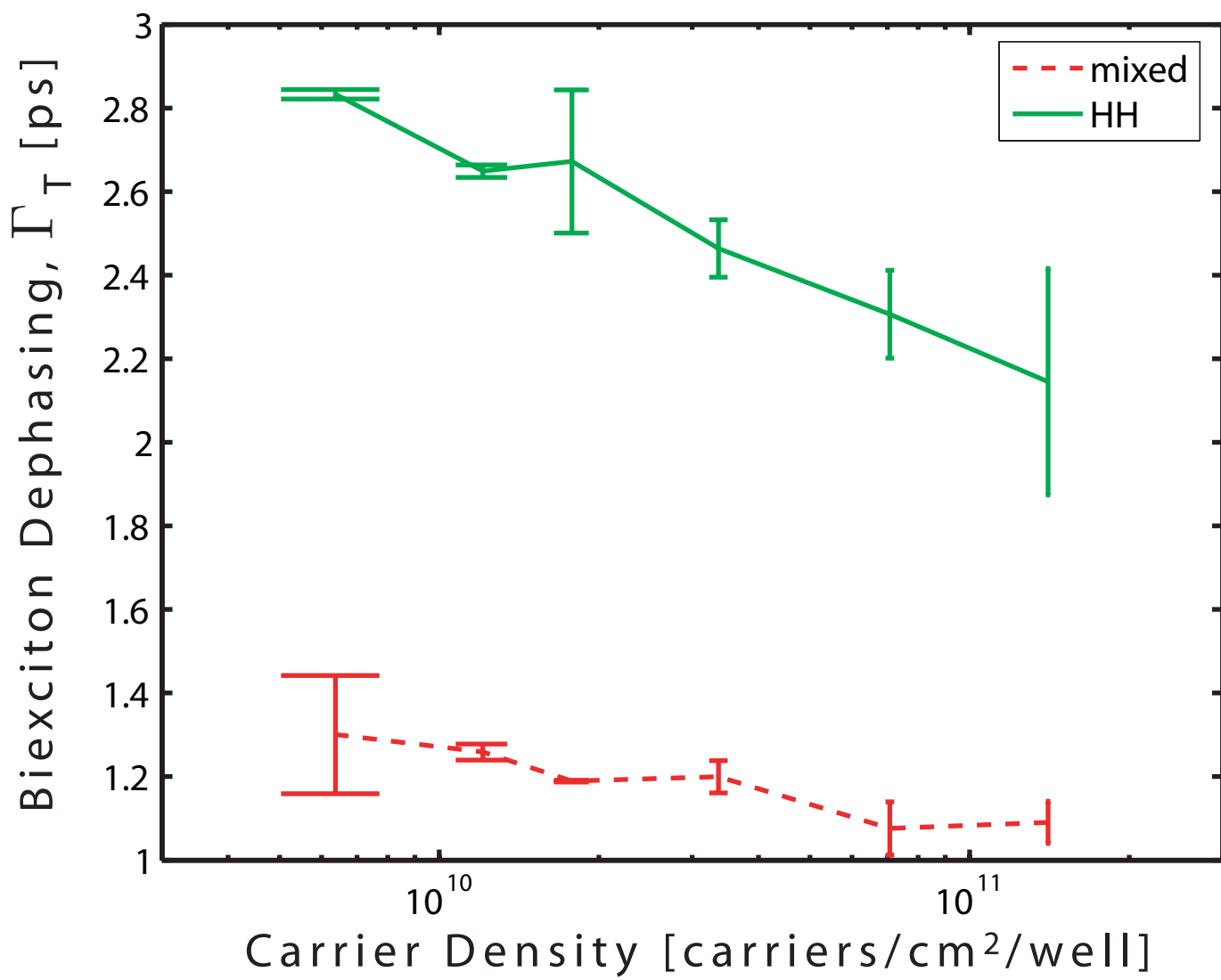
Fig. 1.

Fig. 2.

Fig. 3.

Fig. 4.